2021

Stobe Photography Mapping of Cell Membrane Potential with Nanosecond Resolution

Allen S. Kiester

Bennett L. Ibey

Zachary N. Coker

Andrei G. Pakhomov
Old Dominion University, apakhomo@odu.edu

Joel N. Bixler

Original Publication Citation

Kiester, A. S., Ibey, B. L., Coker, Z. N., Pakhomov, A. G., & Bixler, J. N. (2021). Strobe photography mapping of cell membrane potential with nanosecond resolution. *Bioelectrochemistry*, 142, 1-10, Article 107929. https://doi.org/10.1016/j.bioelechem.2021.107929

Bioelectrochemistry 142 (2021) 107929

Contents lists available at ScienceDirect

Bioelectrochemistry

journal homepage: www.elsevier.com/locate/bioelechem

Strobe photography mapping of cell membrane potential with nanosecond resolution

Allen S. Kiester [a], Bennett L. Ibey [a], Zachary N. Coker [b], Andrei G. Pakhomov [c], Joel N. Bixler [a,*]

[a] Bioeffects Division, Airman System Directorate, 711th Human Performance Wing, Air Force Research Laboratory, JBSA Fort Sam Houston, TX, USA
[b] SAIC, Ft. Sam Houston, TX, USA
[c] Frank Reidy Research Center for Bioelectrics, Old Dominion University, Norfolk, VA, USA

ARTICLE INFO

Article history:
Received 1 October 2020
Received in revised form 7 August 2021
Accepted 10 August 2021
Available online 13 August 2021

Keywords:
FluoVolt™
Strobe photography
Membrane potential
CHO-K1

ABSTRACT

The ability to directly observe membrane potential charging dynamics across a full microscopic field of view is vital for understanding interactions between a biological system and a given electrical stimulus. Accurate empirical knowledge of cell membrane electrodynamics will enable validation of fundamental hypotheses posited by the single shell model, which includes the degree of voltage change across a membrane and cellular sensitivity to external electric field non-uniformity and directionality. To this end, we have developed a high-speed strobe microscopy system with a time resolution of ~ 6 ns that allows us to acquire time-sequential data for temporally repeatable events (non-injurious electrostimulation). The imagery from this system allows for direct comparison of membrane voltage change to both computationally simulated external electric fields and time-dependent membrane charging models. Acquisition of a full microscope field of view enables the selection of data from multiple cell locations experiencing different electrical fields in a single image sequence for analysis. Using this system, more realistic membrane parameters can be estimated from living cells to better inform predictive models. As a proof of concept, we present evidence that within the range of membrane conductivity used in simulation literature, higher values are likely more valid.

1. Introduction

The electrodynamics of cell membranes is fundamental to many biological processes and a critical control parameter for cellular manipulation. A large body of scientific work has been devoted to observing the dynamics of membrane potential during naturally occurring processes including exocytosis, neural action potential, and muscle contraction [1–5]. Confocal and brightfield microscopy, with the addition of fluorescent membrane reporters, enable the widefield monitoring of changes in membrane potential at frame rates on the order of tens of milliseconds [6–12]. While this time regime allows for studying cell to cell communication, it is inadequate to visualize rapid changes in membrane potential that are caused by external electrical stimulation, particularly during the delivery of an electrical pulse [13–17]. Currently, electrical stimulation approaches are being investigated for many purposes including treating inoperable cancer, remote neural stimulation, and biotechnology [18–24]. These and other applications of electrical stimulation justify the need for an improved understanding of membrane charging dynamics and more accurate modeling.

Previous efforts to visualize rapid changes in membrane potential have applied strobe photography and membrane potential dyes to measure the charging in a cell at individual time points [25,26]. Kinosita *et al.* described the use of a pulsed laser fluorescent microscope on sea urchin eggs [26]. In their setup, a 0.3 μs laser pulse was used to illuminate the styryl dye RH292 staining a sea urchin egg membrane. They captured sub-microsecond snapshots of a 20 μs electrical pulse showing membrane charging in agreement with predictions from single shell models. Additionally, they showed that such measurements could be used to approximate dielectric properties from a living cell, specifically membrane conductivity. Frey *et al.* followed up on this seminal work by using a 5 ns duration strobe to generate a series of fluorescent images of Jurkat cells throughout a single 60 ns electrical pulse exposure [25]. The cells were dyed with ANNINE-6, which is a potentiometric dye that embeds itself into the membrane and changes its fluorescent intensity across the biological membrane voltage range [27]. Their work showed that this technique could be used for snapshot imaging of membrane voltage with high temporal resolution. Unfortunately, due to the potential for membrane

* Corresponding author.
E-mail address: joel.bixler.1@us.af.mil (J.N. Bixler).

https://doi.org/10.1016/j.bioelechem.2021.107929
1567-5394/Published by Elsevier B.V.

permeabilization with the exposure used in their study, repeated events were prohibited and only a single image was acquired per cell. Thus, the full sequence of time dynamics required imaging multiple cells at each time point probed to allow for ensemble averaging of the biological variability and dye loading efficiencies from cell to cell. However, the results showed that a single cell exposed to a nanosecond pulsed electric field (nsPEF) will exhibit membrane potential changes on the sides of the cell facing the anode and cathode, a pattern consistent with single shell models.

Our research team achieved even higher temporal resolution than Frey *et al.*, by utilizing streak camera microscopy (SCM) to visualize changes in membrane charting at the nanosecond time regime [14]. This technique used a high-power laser pulse (≥500 mW) to excite FluoVolt™ dye embedded within CHO-K1 cells exposed to nsPEFs of various duration. The fluorescence changes were captured using a streak camera that provided nanosecond-scale visualization of charging dynamics in single-shot acquisitions. This SCM technique offered a substantial advantage over strobe photography in that the complete dynamics of the membrane response to the nsPEF was captured for each acquisition, enabling the study of single-cell charging dynamics. The data generated by this technique is the first to show real time membrane charging and discharging at the poles of a cell with nanosecond time resolution. These data were compared to a single shell model and showed good agreement. However, SCM allows only one spatial dimension (for anode and cathode) and is relegated to single cell analysis.

While both of these high-speed imaging approaches were validated using unipolar nsPEF stimulation, their utility for understanding the plasma membrane charging dynamics during a single bipolar and/or pulsed alternating current (AC) stimulus is compelling. Multiple studies have shown that single bipolar nsPEFs induce significantly less membrane permeabilization as compared to an equivalent or even double duration unipolar nsPEF [28,29]. This experimental observation was not predicted by existing theoretical models of membrane permeabilization and is in stark contrast to millisecond and microsecond duration exposures, where similar levels of permeabilization are observed for bipolar pulses. These observations necessitate that models be advanced to explain such results, and core to those advancements is quantifiable empirical data and visualization of cell membrane electrodynamics under relevant stimuli. Beyond nsPEF bipolar stimulation, the charging and discharging kinetics of high frequency AC waveforms is also not fully understood as it applies to use for novel stimulation and disease treatments [30–32]. Mir et al. recently evaluated the Chinese hamster lung cell line DC-3 response to AC exposures by measuring permeabilization effectiveness, with Fluo-4 calcium measurement for 8–130 kHz AC waveforms [33]. Their data used standard fluorescence microscopy and was limited to imaging calcium response every 5 s but showed the loss of efficiency expected with increasing frequency. Additionally, numerous papers focusing on high frequency irreversible electroporation have shown significant differences in effectiveness with varying frequency, pulse shape, and interpulse interval [34–36]. While mostly in the microsecond regime, such data along with bipolar nsPEF results highlights the need to better understand membrane charging kinetics during such exposures to optimize biological outcomes and minimize electrical overexposures.

Toward this goal, our team has constructed a strobe photography system with nanosecond temporal resolution and wide sample illumination within the microscope field of view. This strobe photography system was utilized to acquire series of images during a repeated electrical stimulus (delivered by a pair of tungsten electrodes). We obtain a single image of membrane charging for each time point with respect to the electrical stimulus exposure by shifting the timing of the laser excitation with respect to the repeated electrical stimulus for each image in the series. In this report, we present membrane charging for CHO-K1 cells, stained with FluoVolt™ dye, exposed to sinusoidal waveforms at 100 kHz, 500 kHz, and 1 MHz. These results show good agreement when compared to a single shell model. These data support the use of this technique across many different regimes of electrostimulation or any rapid stress that would induce a change in membrane potential. The strobe technique retains a temporal resolution advantage over confocal fluorescence imaging or other comparable techniques when used for observing slower changes in membrane potential (~0.5 to ~ 10 ms) and affords an added spatial dimension advantage (2D versus 1D) over techniques applicable to faster changes.

2. Materials and methods

2.1. Strobe system

A strobe microscopy system was designed to provide maximal fluorescence excitation for FluoVolt™ using a nanosecond pulsed laser (Fig. 1). The optical strobe was generated from a cuvette dye cell containing Coumarin 440 (Luxottica Exciton, USA) optically pumped with the third harmonic from a Q-switched neodymium-doped yttrium aluminum garnet (Nd:YAG) laser with a ~ 6 ns pulse width (Centurion, Quantel Lasers, USA) . The laser beam was directed to the cuvette via two harmonic separators (BSR-35–1025, CVI Laser Optics, USA) ensuring complete suppression of the first and second harmonics. The 440 nm strobe pulses were fiber launched into a large core (600 μm), low OH, multimode fiber (M53L02, Thorlabs, USA), providing filtration of the 355 nm laser excitation, and directed to the rear epifluorescence port of an inverted microscope (IX73, Olympus, USA). The average pulse energy delivered to the microscope was 30 μJ with a standard deviation of 0.254 μJ recorded (Coherent LABMAX TOP energy meter with a Coherent J-10 MB-LE sensor) from 100 pulses at 18 Hz. A 488 nm dichroic and long pass filter cube (LPD02-488RU, LP02-488RU, Semrock, USA) was used to direct excitation to the sample stage and transmit the emission to the camera. Event timing was controlled by a digital delay generator (DG645, Stanford Research Systems, Sunnyvale, CA.), which was triggered by the Q-switch of the Nd:YAG laser.

For each image sequence, the DG645 would vary the timing between the laser pulse, camera, and electrical pulse delivery for predefined time increments to sample different portions of the exposure waveform, for a total of 40 pulses and image acquisitions per sequence. This process is further discussed in section 2.3. The timing uncertainty was <5 ns, caused by laser jitter. The maximum image acquisition rate was 18 Hz, limited by the maximum rate at which the delay generator could be written to from LabVIEW, resulting in each image sequence being captured in ~ 2.2 s. All images were acquired with a 40X microscope objective (UPLXAPO40XO, NA 1.4, Olympus, USA). A slightly offset telescope was used to add divergence prior to launching the beam into the microscope to prevent tight focusing of the excitation source by the objective and providing a wider illumination at the sample. This resulted in a beam spot centered in the microscope field of view with a 228 μm full-width half-max diameter, defining the "full field of view" referred to in this manuscript. Control of the laser and programing of the DG645 was handled by a custom LabVIEW (National Instruments, USA) application.

2.2. Cell lines and staining

The experiments were conducted with CHO-K1 cells (ATCC® CCL-61™, Chinese hamster ovary). Cells were maintained at 37 °C

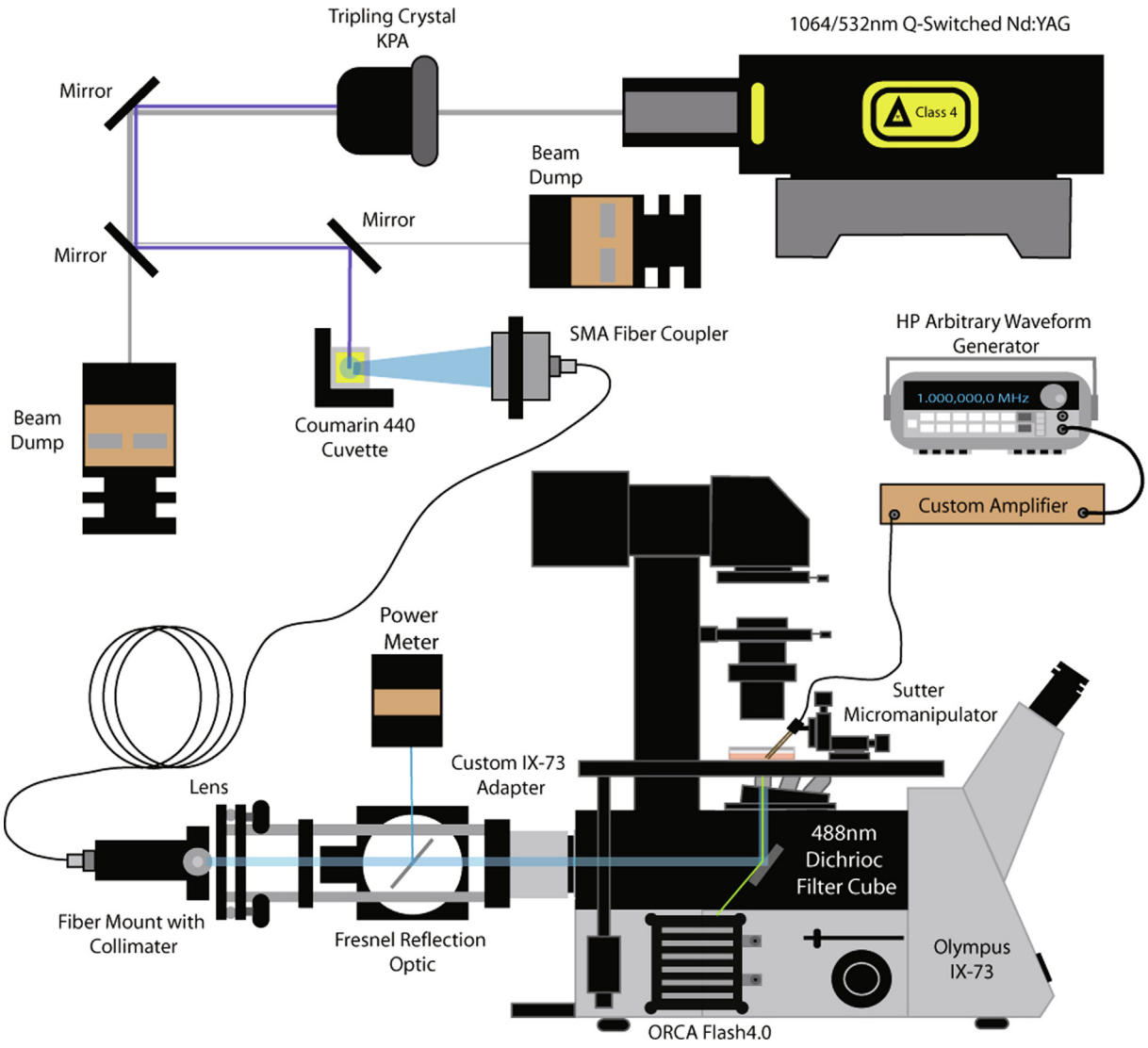

Fig. 1. Strobe Photography Schematic. The 1064 nm output of a Q-switched Nd:YAG laser (Quantel Centurion+) was tripled to 354 nm using a KPA crystal and directed via three beamsplitters (CVI BSR-35-1025) into a cuvette containing Coumarin 440 laser dye dissolved in methanol, generating a 440 nm 6 ns pulse. The strobe pulse was then fiber launched and coupled into the rear epi-fluorescence port of an IX73 microscope (Olympus, USA). A Fresnel reflector (microscope slide) was placed in the beam path in order to direct a small portion of the strobe pulse to an energy meter. The 440 nm light was directed to the sample stage by a 488 nm dichroic beamsplitter (Semrock LPD02-488RU). The resultant fluorescent image was further filtered by a long pass filter (Semrock LP02-488RU) and captured by an ORCA-Flash4.0 V.3 sCMOS camera at an 18 Hz rate resulting in a series of images taken sequentially at different times during the AC stimulus.

with 5% CO_2 in air with relative humidity of about 95%. The CHO-K1 cell line was propagated in Kaighn's Modification of Ham's F-12 Medium (F-12 K Medium). Cell culture media was supplemented with 10% fetal bovine serum (FBS, ATCC® 30-2020™), 2 mM L-glutamine, and 1% volume 100 U/mL penicillin/streptomycin (ATCC® 30–2300) following the guidelines set forth by the provider. All cells were obtained from American Type Culture Collection [ATCC] (Manassas, VA).

Cells were plated onto an imaging dish (μ-Dish 35 mm, low Grid-500; Ibidi™ GmbH, Martinsried, Germany) three hours before imaging. 30 min prior to imaging, the cells were rinsed and loaded with FluoVolt™ Membrane Potential Kit (Cat: F10488, ThermoFisher Scientific, USA) in physiological buffer solution with 10 μL of 100X PowerLoad™ concentrate and 1 μL of FluoVolt™ dye per mL of buffer solution following the manufacturer's protocol. The buffer solution was prepared in advance and contained 135 mM NaCl, 5 mM KCl, 10 mM HEPES, 10 mM glucose, 2 mM $CaCl_2$, and 2 mM $MgCl_2$ with a pH of 7.4 and osmolality of 290–310 Osm/kg (all from Sigma-Aldrich, USA). Cells were then placed back into the incubator for 30 min to allow time for the dye to load properly. The cells were rinsed with fresh buffer solution to remove excess dye and imaged within 30 min of staining. The average diameter of cells imaged was 12.0 ± 1.2 μm.

2.3. Sinusoidal pulse delivery

The single sinusoidal pulse was delivered to cells by 120 μm diameter tungsten electrodes with ~ 350 μm separation, placed directly on the coverslip. The electrodes were carefully positioned using a micromanipulator (MP-225, Sutter Instruments, USA) to both ensure repeatability of positioning, and to avoid physical contact with cells of interest. A custom bipolar amplifier generated the sinusoidal pulses using a high-power operational amplifier (Apex PB64, Apex Microtechnology, USA) with a seed signal produced by a function generator (Agilent HP 33120A, Keysight Technologies, USA). Frequencies of 100 kHz, 500 kHz, and 1 MHz were delivered in bursts of 40 pulses for each image acquisition sequence with an amplitude of ± 45 V at the electrodes. The laser and camera

were triggered at time delays relative to the sinusoid frequency and were selected to provide 5 images pre-exposure, 13 images post-exposure, and evenly sample a single period of the applied signal. The images pre- and post-exposure are used for bleaching correction.

2.4. Simulation

The directionality and strength of the applied electric fields were simulated using COMSOL Multiphysics® (Figs. 2(b,c) and 4 (a,b)), and the voltage used in simulations was set to match the voltage applied to our electrodes (±45 V). The electrode dimensions used for the simulation were determined from bright field images and distance calibration calculated using the 1951 USAF glass slide resolution target (Edmund Optics, USA). Estimated field intensity was fed into a single shell dielectric sphere model for membrane charging to estimate expected cell response [30,37–40].

2.5. Data processing

To analyze image sequences acquired by this system, it is necessary to compensate for photobleaching of the fluorescent dye that occurs from exposure to multiple laser pulses. To do this, we use the fact that no charging should occur at the 90° and 270° poles of each cell with respect to the applied electric field. This assumption can be validated by modeling the predicted voltage change at these points using a single shell model, as shown in Fig. 4(d) and as discussed later in this manuscript. Thus, changes in the FluoVolt™ intensity at these points should not be impacted by induced membrane voltage variations but should be dominated by photobleaching. To generate a bleaching correction curve, we first select a 3-

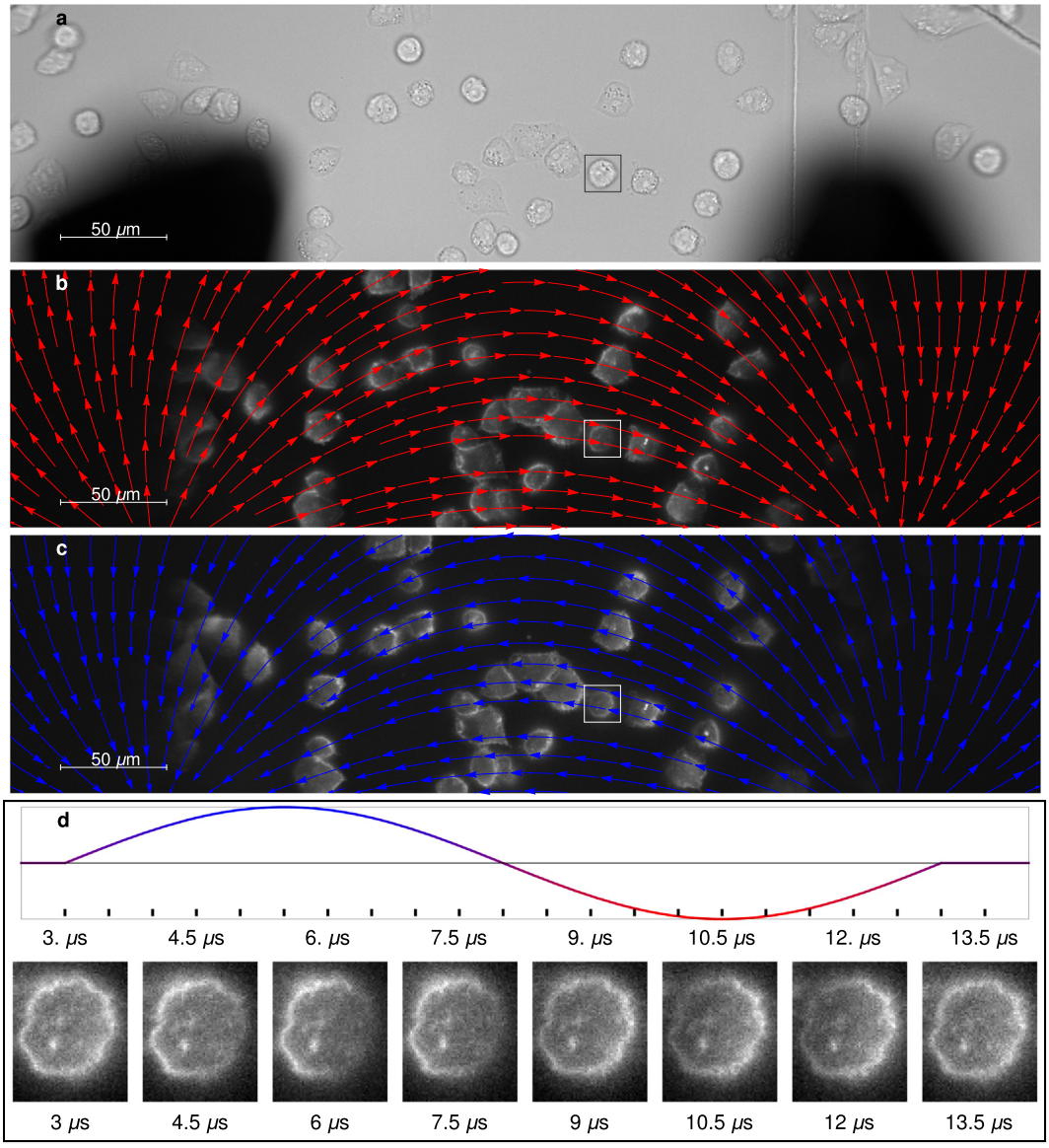

Fig. 2. Representative field of view with electric field directionality. (a) Brightfield image of CHO-K1 cells between two tungsten electrodes. (b, c) Modeling results from COMSOL Multiphysics® simulation of the exposure geometry represented as overlaid field directionality lines on a fluorescent image of CHO-K1 cells labeled with FluoVolt™ dye. (d) Single cell images are shown across 8 time points for 100 kHz single sinusoidal exposures for a cell located within the white box (c) directly between the electrodes. The sinusoid shown in the top panel of (d) is representative of amplitude of the waveform shown with an arbitrary magnitude (volts). FluoVolt™ intensity changes at the edges of the cells show charging and discharging dynamics as predicted during a single AC oscillation. The ticks are representative of when strobe pulses occurred in each of the 40 electrical pulses applied to the cell, one strobe pulse per electrical pulse (Not shown are ticks for 5 additional strobe images captured prior to the sinusoid, and 13 additional strobe pulses after the end of the sinusoid).

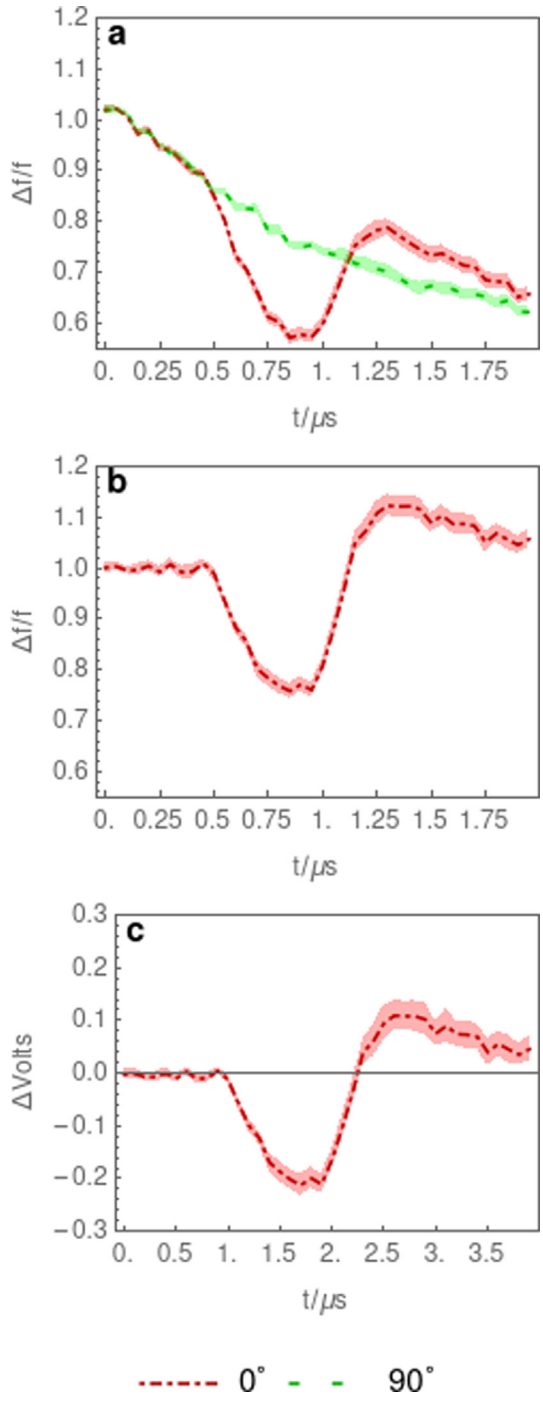

Fig. 3. Compensation for photobleaching artifacts in strobe photography data. (a) Raw comparison between the 1 MHz AC fluorescence response average of 15 cells aligned to the field (0°) and perpendicular (90°). Loss of fluorescence intensity in both locations is seen due to the intense laser stimulation across 40 independent exposures at 18fps. (b) Compensation of the photobleaching using the perpendicular (90°) response. (c) Conversion of the data from ΔF/F to membrane potential (ΔV) using previously obtained patch clamp FluoVolt™ calibration data [14]. Curves represent the average of 10 cell responses and the shaded region represents ± standard error of the mean.

pixel radius circular region of interest (ROI) at the 90° pole of each cell analyzed and normalize this ROI using the first 5 frames per image sequence. The normalized intensity for this ROI is then averaged for all cell image sequences analyzed within a given dataset, producing a bleaching correction curve. We can then divide individual cell image sequences by this curve to remove the effects of photobleaching.

Fig. 3(a) shows a representative plot of the mean florescent intensity over time for 15 cells at 0° and 90° relative to the applied electric field. The results of the bleaching compensation are shown for signal at 0° relative to the field in Fig. 3(b). The impact this procedure has on the standard error is included via the error band shown in Fig. 3(a-c) plotted as the square root of the sum of the squared errors for both 0° and 90°. This method preserves the statistical error at both ROIs. A feature worth noting is the growth of the error over time because, intrinsically, photobleaching reduces the signal to noise ratio. Conversions of change in fluorescence intensity (reported as a percent change) to change in membrane voltage was preformed using the same method and patch clamp electrophysiology data previously discussed in Beier *et al.* [14]. A representative example is shown in Fig. 3(c).

2.6. Single shell model

The single shell capacitive response model proposed by Kotnik *et al.* [38] was used as an analytical model to compare to our experimental results. The model assumes three domains each characterized by a relative dielectric permittivity ε (as a factor of the vacuum permittivity $\varepsilon_0 = 8.85\text{x}10^{-12}s^4A^2/kgm^3$) and electrical conductivity λ: ε_e (80 ε_o) and λ_e (1.45 S/m) for outside the shell (the extracellular medium); ε_m (5 ε_o) and λ_m ($3x10^{-7}$S/m) for the shell itself (the cell membrane); ε_i (80 ε_o) and λ_i (0.3 S/m) for inside the shell (the cytoplasm). λ_e is the measured conductivity of our media and all other values are unknown or found in literature [7,8,10,15]. To calculate the time dependent charging response of a spherical membrane to an external electric field, we use the solution of the Laplace's equation for sinusoidal electric fields,

$$\nabla^2\Phi_m\left(\vec{r},t\right) = fE(t)Rcos(\theta), \tag{1}$$

as calculated by Kotnik *et al.* [38] but not included for brevity. The parameters are as follows: $\Phi_m(r,t)$is defined as the potential of the cellular membrane; $E(t)$ is the time varying but spatially uniform applied electric field predicted by COMSOL; R the radius of the cell; and f is a geometric function calculated by matching the boundary conditions between the membrane and both the external media and cytoplasm, given as:

$$\begin{aligned} f = {} & 3\lambda_e(3dR^2\lambda_i \\ & + \left(3d^2R - d^3\right)(\lambda_m - \lambda_i))/(2R^3(\lambda_m + 2\lambda_e)\left(\lambda_m + \frac{1}{2}\lambda_i\right) \\ & - 2(\mathrm{R} - d)^3(\lambda_e - \lambda_m)(\lambda_i - \lambda_m)). \end{aligned} \tag{2}$$

The additional parameter in f, d, is the thickness of the membrane.

3. Results

Predicted field maps for an area matching the microscope field of view using COMSOL Multiphysics® were generated to estimate the field amplitude and direction. Fig. 2(a) shows a bright field image of the electrodes and CHO-K1 cells. This exposure geometry results in a perpendicular field direction between the electrodes with angled field lines at positions further away, highlighting the highly non-uniform field profile generated from the two-electrode configuration for our bipolar stimulation, as shown in Fig. 2(b & c). Previous research using similar exposure conditions has traditionally included only the analysis of cells located directly between the electrodes, where field direction is orthogonal and amplitude is maximized, as to avoid complexities associated with

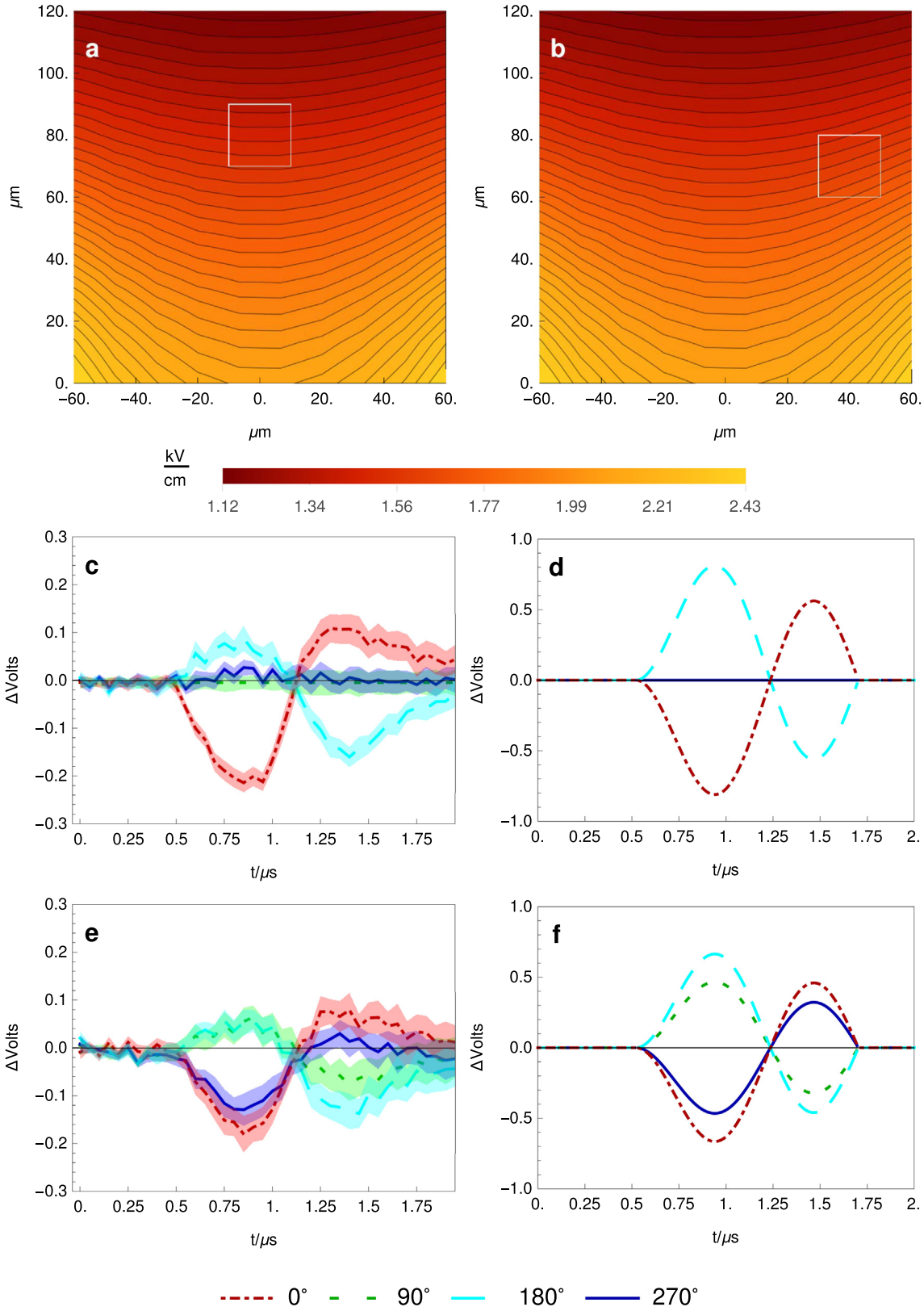

Fig. 4. Full field of view mapping of cellular response to AC stimulus by bipolar electrodes. COMSOL Multiphysics® modeling shows the field magnitude and directionality for the entire field of view 6 μm above the microscope slide (a). Cells were selected within two regions of interest to demonstrate the power of this technique for in vitro stimulation. The first location (a) is in a region where the electric field is perpendicular to the electrodes. Resultant analysis (c) shows highest change in membrane potential perpendicular to the electrodes (0,180) and no response parallel (90, 270). The second cell site (b), where the field directionality is not perpendicular to the electrodes, but rotated 35° relative to the image orientation, shows non-orthogonal charging (e) of the cell membrane. Comparison to single shell model (d,f) for each cell site shows good agreement in general direction of charging. Each empirical measurement consists of the average of 15 cells across 5 plate preparations. The shaded region represents ± standard error of the mean. A legend for the radial orientation for the image is shown in (a) and this orientation is maintained for the image shown in (b). The electric field intensity shown in (a) and (b) varies from 1.12 kV/cm (dark red) to 2.43 kV/cm (yellow).

this non-uniformity [41–43]. By incorporating the complete electrical field of view into image analysis rather than limiting analysis to the region between the electrodes, information can be extracted from a maximum number of cells, thereby providing a more complete understanding of a given exposure outcome.

To demonstrate system capability, we exposed cells to a 100 kHz sinusoid waveform and acquired images at 1.5 μs intervals relative to the start of the sinusoid. For this, a complete image sequence involved 40 exposures, where each individual frame (n = 1 to 40) in the sequency was captured at a time delay, *t*, of 1.5 μs relative to the previous frame ($t(n+1) = t(n) + 1.5\ \mu s$; where $t(n=1) = \sin(0)$ referenced to the sinusoid amplitude). Fig. 2(b & c) show a single fluorescence image at the peaks of the single oscillation ($\sin(\pi/2)$ and $\sin(3\pi/2)$). The field direction is presented as red for the "positive voltage" and blue for the "negative voltage" relative to the initial anode and cathode electrodes. As expected, the field amplitude is identical for both phases of the waveform with a 180° direction change. Furthermore, acquiring the full field of view affords complete analysis of membrane charging for cells within 80% of the beam spot, simultaneously. The capability to analyze a larger number of cells across the full field of view is powerful, and can manifest either as higher throughput with corrective factors applied to the field strength and amplitude, or as a comparative study where differential field strength and orientation are studied across an array of cells within a single time series.

FluoVolt™ is a photo-induced electron transfer dye comprised of an electron donation complex connected to the fluorophore by a molecular wire [44]. When embedded into the plasma membrane, changes in the membrane potential alter the flow of quenching electrons along the molecular wire to the fluorescence reporter, thus modulating the probability of fluorescent emission. In short, if the membrane is depolarized, electrons will not move to the fluorophore and quenching of the dye will be relaxed resulting in more fluorescent emission. The opposite occurs in hyperpolarization, where more electrons move to the fluorophore thus quench the emission process. Previous work with SCM confirmed that FluoVolt™ has a sub-microsecond response time to membrane charging by resolving the kinetics of a 600 ns pulse exposure in a living cell with a time resolution of < 10 ns [14]. In the first half of Fig. 2(d) ($time < 8\ \mu s$) the cell is positioned between the electrodes with the anodic electrode on the right side and the cathodic electrode on the left side. The fluorescence intensity of the cell is brighter towards the cathodic electrode (corresponding to depolarization of the cells membrane) and dimmer towards the anodic electrode (corresponding to hyperpolarization). The applied pulse is bipolar, both electrodes serve as the cathode and anode in turn. In the second half of the pulse ($time > 8\ \mu s$) the cathodic and anodic electrodes are reversed as are the bright and dim sides of the cell.

We analyzed 15 cells across 5 exposures in two distinct locations, as shown in the white boxes in Fig. 4(a & b) to demonstrate the impact of spatial proximity between the electrodes and cells. Fig. 4(a) depicts a position between the electrodes where the electric field lines would be perpendicular to the poles (top and bottom) of a cell. Cells within this region were pulsed with a single 1 MHz sine wave per image for 40 images, and the mean percent change in fluorescent intensity was calculated at radial positions along the cell membrane of 0°, 90°, 180°, and 270° relative to the image orientation, shown in the legend in Fig. 4(a). This experiment was repeated across five separate culture dishes over the course of multiple days. Fig. 4(c) shows the average time traces of the membrane potential of cells exposed in this region. As expected, the observed charging and discharging dynamics of the membrane align with the predicted field direction (Fig. 2(b & c)) on either side of the cell and the poles (90°, 270°) experience no change in membrane potential. For cells placed closer to the cathode, the field lines were not perpendicular relative to the image orientation but were rotated by ~ 35° and the field was approximately 18% stronger (Fig. 4(b)). Membrane charging for cells within this ROI is plotted in Fig. 4(e), where charging is observed at the 90° and 270° points due to the rotated field. Despite the stronger field, the magnitude of membrane charging observed at this location is comparable to that seen in Fig. 4(c) because we are not analyzing points that are directly aligned with the applied field. This analysis can be performed for all cells within the field of view relative to the applied field directionality to create an overall cell response for equipotential regions at different spatial locations and for areas of different electric field intensity or arbitrary angle relative to the field. Applying a single shell model of cell membrane charging, we show the expected response of each cell region (Fig. 4 (d & f). Good agreement is seen in the overall trend of the empirical data as compared to the single shell model results. It should be noted that the observed cellular response follows a similar anode and cathode asymmetry as seen in previous work, including single-shot techniques such as SCM [14,45].

4. Discussion

Strobe photography allows for 2D visualization of the cell membrane response to sub-microsecond electrical stimuli with nanosecond time resolution, a dramatic improvement over streak photography which is limited to a single spatial dimension. This technique can be applied to study a variety of electrical stimulation geometries or other stimulation (optical, acoustic, thermal) that may result in a rapid change in membrane potential. Strobe photography has previously been used to show the dynamic changes in membrane potential for single cells during nanosecond electrical pulse exposures using ANINE-6 dye, and conclusively showed that cell membranes are capable of charging in response to high amplitude nanosecond duration fields and that this charging agrees with single cell model predictions [25]. Our paper is a natural extension of the work presented by Frey *et al.*, with the addition of a full field of view to the technique (allowing for analysis of a large number of cells per acquisition), improved signal to noise primarily from the more efficient dye and more sensitive detector, and measured membrane potential changes for a range of frequencies. One key advancement is the use of FluoVolt™ membrane potential dye as a reporter as compared to ANINE-6. FluoVolt™ offers superior quantum efficiency as compared to previously studied potentiometric dyes. Additionally, this dye has been shown to have sub 10 ns response time in living cells with a linear response to membrane charging from −100 to +80 mV, thus making the dye ideal for cell studies matching the normal physiological range of membrane potential [44]. Additionally, advances in sCMOS cameras have enabled the rapid acquisition of full frame images at rates up to 100 Hz, with quantum efficiencies that can approach 95% [15], affording opportunities to further increase image sequence acquisition. The combination of a more responsive dye and more sensitive camera technology enabled the acquisition of repeated full field of view images by reducing the needed laser excitation energy, and thus reducing sample damage.

Previous attempts to use strobe photography on a living system have proved challenging, as the biology may change upon the first stimulation event and subsequent exposures may therefore measure an altered system. Previous work acquired a single image for a single time point during the stimulation of a single cell to avoid this potential complexity [25]. This approach required a high number of cells to be analyzed individually to build up an accurate picture of the total temporal cell response and was therefore confounded by biological variability and fluorescent dye uptake between individual cells in a population. Significant error could affect such measurements, as cells vary in shape, membrane poten-

tial, and additional factors including the active stage of the cell cycle and overall health. Our system enables complete temporal acquisition of the image stack on a single set of cells across the entire field of view. This use of strobe photography will inherently have limitations for very high amplitude exposures that can cause disruption of the plasma membrane or even electroporation resulting in a nearly immediate change in the dynamics of membrane potential. Membrane potential changes following high amplitude single nanosecond duration exposures have been observed immediately after the exposure (within nanoseconds) as demonstrated recently by Streak Camera Microscopy [46]. Therefore, we believe the strobe imaging technique has the highest utility for measuring the dynamics of membrane charging during electrical stimulus in non-injurious, low to moderate dose regimes where electropermeabilization is not expected. Specifically, in Fig. 4(c & e), we notice an increase in the standard error of the signals as the acquisition time increases. This increase is easiest to visualize in the red 0° trace in Fig. 4(c). This can likely be explained primarily due to the bleaching of the dye, where the decrease in fluorescence intensity follows the same trend as the increase in standard error. It is possible the short-to-long order of exposure in our experimental design may have contributed to the increase in standard error as well. This is notable as the time delay was performed from shortest to longest along the sinusoidal profile. While our single pulse amplitude is not considered "high", given the frequency, subsequent multiple exposures could possibly create membrane damage and impact the membrane potential. It is also likely that the muted response we see in the recovery is not completely real, but a combination of the change in membrane potential of the cell and the accumulation of damage or chemical species altering the local environment around the cell. It must also be noted that the laser irradiance, although brief and infrequent, is intense, and photodamage to the dye, the cell, or generation of chemical species in the sample is also a confounding issue that would impact acquisition of more time points per exposure set. This could be minimized by limited the number of time steps for the acquisition, specifically, for longer duration or lower frequency exposures. We are currently modifying our acquisition protocol to acquire images at random times through the exposure rather than collecting in sequential order with respect to pulse position. This change will serve to more randomly distribute the error observed across all time points, which can then be addressed more easily using a moving average filter.

Beyond single event temporal mapping, as executed in this study, the strobe technique can enable very precise timing of repeated events such as multiple single pulse exposure by simply leaving the timing fixed and recording at a precise time point for each pulse. Previous work investigating multiple exposure scenarios has required a significant time between each pulse application to resolve the cell response prior to the next pulse application. This ultimately limits the technique to measuring a single response after a train of pulses, or slowing the repetition rate down significantly to resolve single pulse additivity [47,48]. However, as the timeframe for cellular response to fields is likely at the microsecond time scale, anything resolving changes with insufficient frame rates is likely probing an indirect cell-driven response, muddying the analysis of the exposure. Recent data has shown that very low amplitude nanosecond duration pulses applied at MHz repetition rates can ultimately manifest in electropermeabilization of the plasma membrane [49]. This effect is absent in exposures with kHz repetition rates despite having the same number of pulses. This observation points to an additivity that is time dependent and on the order of the charging time of the cell membrane (predicted to 10-100's of nanoseconds). We intend to apply strobe photography to analyze the change in membrane potential at the onset of each pulse within this train. Strobe microscopy enables both high temporal resolution and long overall exposure duration; such data cannot be acquired using other imaging modalities. Validation of how the cell "charges" to the critical breakdown voltage from low amplitude rapid exposures will enable optimization of this effect for its ultimate use in clinical therapy.

When compared with single cell model results, we find that overall response kinetics of cells between and away from the electrodes are predicted properly. However, the predicted voltage change is considerably higher than measured. As discussed earlier in this section, there are a number of confounders that may be impacting the cell response. For example, the constraints of our imaging technique necessitate that the cells are undergoing a multiple exposure scenario that we are effectively combining and comparing to a single exposure condition. Membrane breakdown, biological/chemical reactions, and fluorescent reporter damage would all cause underreporting of the peak membrane potential as compared to an idealistic charging model. Additionally, as shown in our previous paper using SCM, which captures the entire charging event in a single shot and thus avoids most of the confounding issues of strobe photography, FluoVolt™ reporting was nearly 50% below that predicted by a similar model [14]. Given that two techniques have both shown that the membrane potential, as measured by FluoVolt™ during nanosecond duration electrical stimuli, is lower than predicted, it is likely that either our calibration of FluoVolt™ is not entirely accurate for a dynamic system (static measurements taken using patch clamp electrophysiology) or that the dielectric properties (membrane permittivity and conductivity) being used within the model deviate somewhat from the true biological values.

While validation of membrane dielectric properties is beyond the scope of this paper, we believe that empirically measured strobe charging dynamics could validate predictions of frequency dependent dielectric properties in cells [11]. The modeling results in Fig. 4(d & f) were generated using properties extracted from literature and showed good directional correlation, but poor amplitude prediction [38,50]. We, therefore, modified our modeling parameters to better match the empirical data (Fig. 4(c & e)). We found that membrane conductivity appears to be the most influential parameter and achieved the best fit (Fig. 5). In literature, this value varies considerably ($1 \times 10^{-7} - 1 \times 10^{-2}$ S/m) suggesting that the true value is not known and that variability across different cells lines and at different frequencies is not well characterized [33]. Membrane conductivity is dependent on the conductivity of the external medium. Minimal literature was found measuring membrane conductivity in a media with conductivity at or around 1.45 S/m (as used in our cell study), despite numerus measurements in media with lower conductivity [50–54]. We used the single shell model to fit our empirical data and predicted a higher membrane conductivity. The value predicted based on the empirical data was a good fit across all three frequencies, suggesting minimal frequency dependence of this parameter in the frequency range explored. Additionally, we also noted a slight phase shift in our data relative to the modeling prediction. This phase shift over the course of multiple exposures would suggest that we may have induced a change in the electrical properties of the cell (possibly due to minor or accumulated cell injury across repeated exposures). While this is a confounder as compared to the model, it underscores the power of this technique to evaluate cell response to rapidly applied multiple exposures, specifically high frequency AC bursts too fast to be captured by standard microscopy. This simple empirical validation of modeling parameters underscores our goal of expanding this technique into different exposure scenarios to ultimately make quantitative measurements of the dynamic electrical properties in living cells. Our team believes that the lack

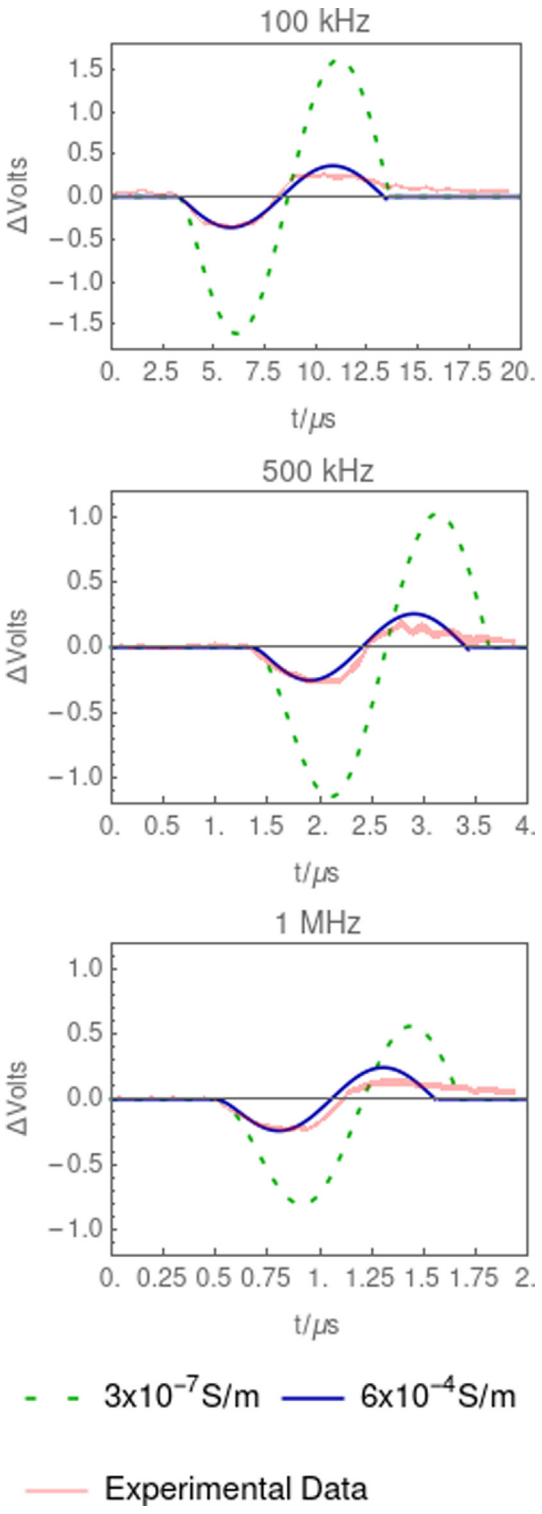

Fig. 5. Using Strobe Photography images to predict membrane conductivity in living cells. Results for two membrane conductivity values are presented for all three frequencies under test (100 kHz (n = 10 cells), 500 kHz (n = 10 cells), and 1 MHz (n = 15 cells)). Poor agreement in amplitude is observed when a membrane conductivity of 3×10^{-7} S/m is used to simulate membrane charging. Multiple modeling experiments resulted in a membrane conductivity of 6×10^{-4} S/m as a good approximation derived from our empirical data. Loss of fit over time is likely due to membrane injury by the intense laser exposure and repeated AC stimulation. The shaded region represents the ± standard error of the mean.

of such time and intensity varying electrical parameters of living systems is one major reason why current models fall short of accurately predicting biological outcomes [28,55,56].

5. Conclusion

In conclusion, our research team has demonstrated a novel application for strobe photography to measure dynamic changes in living cells across a wide field of view. This technique was used to capture membrane potential dynamics in cells exposed to a low amplitude sinusoidal waveform using bipolar stimulating electrodes. We believe that this technique can be applied more generally to many exposure geometries, exposure scenarios, and to a variety of living targets, including cells, brain slices, and *in vivo* preparations. Future work will employ this technique to validate the dielectric properties of living cells for kHz to MHz frequencies, rapid delivery of low amplitude nanosecond pulses, and membrane changes due to fast thermal gradients brought about by infrared laser exposures.

Declaration of Competing Interest

The authors declare that they have no known competing financial interests or personal relationships that could have appeared to influence the work reported in this paper.

Acknowledgements

Work contributed by SAIC was performed under USAF Contract No. FA8650-19-C-6024. Additional support for ASK was provided through the Oak Ridge Institute for Science and Education (ORISE). Funding for this work was provided through AFOSR Grants 17RHCOR483 and 20RHCOR051.

References

[1] L.-G. Wu, E. Hamid, W. Shin, H.-C. Chiang, Exocytosis and endocytosis: Modes, functions, and coupling mechanisms*, Annu. Rev. Physiol. 76 (1) (2014) 301–331, https://doi.org/10.1146/annurev-physiol-021113-170305.
[2] K. Mukund, S. Subramaniam, Skeletal muscle: A review of molecular structure and function, in health and disease, Wiley Interdiscip. Rev. Syst. Biol. Med. 12 (2020) e1462–e1462. https://doi.org/10.1002/wsbm.1462.
[3] R. Wallace, Neural membrane signaling platforms, Int. J. Mol. Sci. 11 (2010) 2421–2442, https://doi.org/10.3390/ijms11062421.
[4] D.S. Peterka, H. Takahashi, R. Yuste, Imaging voltage in neurons, Neuron 69 (1) (2011) 9–21, https://doi.org/10.1016/j.neuron.2010.12.010.
[5] J.N.D. Kerr, W. Denk, Imaging in vivo: Watching the brain in action, Nat. Rev. Neurosci. 9 (3) (2008) 195–205, https://doi.org/10.1038/nrn2338.
[6] P.E. Deal, V. Grenier, R.U. Kulkarni, P. Liu, A.S. Walker, E.W. Miller, Making Life Visible: Fluorescent Indicators to Probe Membrane Potential, in: Make Life Visible, Springer Singapore, 2020: pp. 89–104. https://doi.org/10.1007/978-981-13-7908-6_9.
[7] P. Liu, E.W. Miller, Electrophysiology, unplugged: imaging membrane potential with fluorescent indicators, Acc. Chem. Res. 53 (1) (2020) 11–19, https://doi.org/10.1021/acs.accounts.9b00514.
[8] D. Gross, L.M. Loew, W.W. Webb, Optical imaging of cell membrane potential changes induced by applied electric fields, Biophys. J. 50 (2) (1986) 339–348, https://doi.org/10.1016/S0006-3495(86)83467-1.
[9] L.B. Cohen, B.M. Salzberg, Optical measurement of membrane potential, Rev. Physiol. Biochem. Pharmacol. 83 (1978) 35–88, https://doi.org/10.1007/3-540-08907-1_2.
[10] G. Pucihar, T. Kotnik, D. Miklavčič, Measuring the induced membrane voltage with Di-8-ANEPPS, J. Vis. Exp. (2009) 1659. https://doi.org/10.3791/1659.
[11] M. Hibino, M. Shigemori, H. Itoh, K. Nagayama, K. Kinosita, Membrane conductance of an electroporated cell analyzed by submicrosecond imaging of transmembrane potential, Biophys. J. 59 (1) (1991) 209–220, https://doi.org/10.1016/S0006-3495(91)82212-3.
[12] B. Ehrenberg, D.L. Farkas, E.N. Fluhler, Z. Lojewska, L.M. Loew, Membrane potential induced by external electric field pulses can be followed with a

potentiometric dye, Biophys. J. 51 (5) (1987) 833–837, https://doi.org/10.1016/S0006-3495(87)83410-0.
[13] H.T. Beier, C.C. Roth, G.P. Tolstykh, B.L. Ibey, Resolving the spatial kinetics of electric pulse-induced ion release, Biochem. Biophys. Res. Commun. 423 (4) (2012) 863–866, https://doi.org/10.1016/j.bbrc.2012.06.055.
[14] H.T. Beier, C.C. Roth, J.N. Bixler, A.V. Sedelnikova, B.L. Ibey, Visualization of dynamic sub-microsecond changes in membrane potential, Biophys. J. 116 (1) (2019) 120–126, https://doi.org/10.1016/j.bpj.2018.11.3129.
[15] H.T. Beier, B.L. Ibey, Experimental comparison of the high-speed imaging performance of an EM-CCD and sCMOS camera in a dynamic live-cell imaging test case, PLoS One. 9 (2014) e84614. https://doi.org/10.1371/journal.pone.0084614.
[16] J. Bradley, R. Luo, T.S. Otis, D.A. DiGregorio, Submillisecond optical reporting of membrane potential in situ using a neuronal tracer dye, J. Neurosci. 29 (29) (2009) 9197–9209.
[17] T.Y. Tsong, Electroporation of cell membranes, Biophys. J. 60 (2) (1991) 297–306.
[18] K.H. Schoenbach, S.J. Beebe, E.S. Buescher, Intracellular effect of ultrashort electrical pulses, Bioelectromagnetics. 22 (6) (2001) 440–448, https://doi.org/10.1002/(ISSN)1521-186X10.1002/bem.v22:610.1002/bem.71.
[19] K.H. Schoenbach, F.E. Peterkin, R.W. Alden, S.J. Beebe, The effect of pulsed electric fields on biological cells: experiments and applications, IEEE Trans. Plasma Sci. 25 (1997) 284–292, https://doi.org/10.1109/27.602501.
[20] R. Nuccitelli, U. Pliquett, X. Chen, W. Ford, R. James Swanson, S.J. Beebe, J.F. Kolb, K.H. Schoenbach, Nanosecond pulsed electric fields cause melanomas to self-destruct, Biochem. Biophys. Res. Commun. 343 (2) (2006) 351–360, https://doi.org/10.1016/j.bbrc.2006.02.181.
[21] A.G. Pakhomov, I. Semenov, M. Casciola, S. Xiao, Neuronal excitation and permeabilization by 200-ns pulsed electric field: An optical membrane potential study with FluoVolt dye, Biochim. Biophys. Acta - Biomembr. 1859 (7) (2017) 1273–1281, https://doi.org/10.1016/j.bbamem.2017.04.016.
[22] M. Casciola, S. Xiao, A.G. Pakhomov, Damage-free peripheral nerve stimulation by 12-ns pulsed electric field, Sci. Rep. 7 (2017) 10453, https://doi.org/10.1038/s41598-017-10282-5.
[23] I. Edhemovic, E.M. Gadzijev, E. Brecelj, D. Miklavcic, B. Kos, A. Zupanic, B. Mali, T. Jarm, D. Pavliha, M. Marcan, G. Gasljevic, V. Gorjup, M. Music, T.P. Vavpotic, M. Cemazar, M. Snoj, G. Sersa, Electrochemotherapy: A new technological approach in treatment of metastases in the liver, Technol. Cancer Res. Treat. 10 (5) (2011) 475–485, https://doi.org/10.7785/tcrt.2012.500224.
[24] R. Nuccitelli, Tissue ablation using nanosecond electric pulses, in: D. Miklavčič (Ed.), Handb. Electroporation, Springer International Publishing, Cham, 2017: pp. 1787–1797. https://doi.org/10.1007/978-3-319-32886-7_93.
[25] W. Frey, J.A. White, R.O. Price, P.F. Blackmore, R.P. Joshi, R. Nuccitelli, S.J. Beebe, K.H. Schoenbach, J.F. Kolb, Plasma membrane voltage changes during nanosecond pulsed electric field exposure, Biophys. J. 90 (10) (2006) 3608–3615, https://doi.org/10.1529/biophysj.105.072777.
[26] K. Kinosita, I. Ashikawa, N. Saita, H. Yoshimura, H. Itoh, K. Nagayama, A. Ikegami, Electroporation of cell membrane visualized under a pulsed-laser fluorescence microscope, Biophys. J. 53 (6) (1988) 1015–1019.
[27] L.H. Wegner, W. Frey, S. Schönwälder, A critical evaluation of whole cell patch clamp studies on electroporation using the voltage sensitive dye ANNINE-6, Bioelectrochemistry 92 (2013) 42–46, https://doi.org/10.1016/j.bioelechem.2013.03.002.
[28] A.G. Pakhomov, I. Semenov, S. Xiao, O.N. Pakhomova, B. Gregory, K.H. Schoenbach, J.C. Ullery, H.T. Beier, S.R. Rajulapati, B.L. Ibey, Cancellation of cellular responses to nanoelectroporation by reversing the stimulus polarity, Cell. Mol. Life Sci. 71 (22) (2014) 4431–4441, https://doi.org/10.1007/s00018-014-1626-z.
[29] B.L. Ibey, J.C. Ullery, O.N. Pakhomova, C.C. Roth, I. Semenov, H.T. Beier, M. Tarango, S. Xiao, K.H. Schoenbach, A.G. Pakhomov, Bipolar nanosecond electric pulses are less efficient at electropermeabilization and killing cells than monopolar pulses, Biochem. Biophys. Res. Commun. 443 (2) (2014) 568–573, https://doi.org/10.1016/j.bbrc.2013.12.004.
[30] C. Grosse, H.P. Schwan, Cellular membrane potentials induced by alternating fields, Biophys. J. 63 (6) (1992) 1632–1642, https://doi.org/10.1016/S0006-3495(92)81740-X.
[31] H. Li, A. Denzi, X. Ma, X. Du, Y. Ning, X. Cheng, F. Apollonio, M. Liberti, J.C.M. Hwang, Distributed Effect in High-Frequency Electroporation of Biological Cells, IEEE Trans. Microw. Theory Tech. 65 (9) (2017) 3503–3511, https://doi.org/10.1109/TMTT.2017.2659736.
[32] S. Katsuki, N. Nomura, H. Koga, H. Akiyama, I. Uchida, S.-I. Abe, Biological Effects of Narrow Band Pulsed Electric Fields 14 (3) (2007) 663–668, https://doi.org/10.1109/TDEI.2007.369529.
[33] T. García-Sánchez, C. Merla, J. Fontaine, A. Muscat, L.M. Mir, Sine wave electropermeabilization reveals the frequency-dependent response of the biological membranes, Biochim. Biophys. Acta - Biomembr. 1860 (5) (2018) 1022–1034, https://doi.org/10.1016/j.bbamem.2018.01.018.
[34] D.C. Sweeney, M. Reberšek, J. Dermol, L. Rems, D. Miklavčič, R.V. Davalos, Quantification of cell membrane permeability induced by monopolar and high-frequency bipolar bursts of electrical pulses, Biochim. Biophys. Acta - Biomembr. 1858 (11) (2016) 2689–2698, https://doi.org/10.1016/j.bbamem.2016.06.024.
[35] T. García-Sánchez, A. Azan, I. Leray, J. Rosell-Ferrer, R. Bragós, M. Ll, Mir, Interpulse multifrequency electrical impedance measurements during electroporation of adherent differentiated myotubes, Bioelectrochemistry 105 (2015) 123–135, https://doi.org/10.1016/j.bioelechem.2015.05.018.
[36] M.B. Sano, C.B. Arena, M.R. DeWitt, D. Saur, R.V. Davalos, In-vitro bipolar nano- and microsecond electro-pulse bursts for irreversible electroporation therapies, Bioelectrochemistry 100 (2014) 69–79, https://doi.org/10.1016/j.bioelechem.2014.07.010.
[37] E. Salimi, K. Braasch, M. Butler, D.J. Thomson, G.E. Bridges, Dielectric model for Chinese hamster ovary cells obtained by dielectrophoresis cytometry, Biomicrofluidics. 10 (1) (2016) 014111, https://doi.org/10.1063/1.4940432.
[38] T. Kotnik, D. Miklavčič, T. Slivnik, Time course of transmembrane voltage induced by time-varying electric fields - A method for theoretical analysis and its application, Bioelectrochem. Bioenerg. 45 (1) (1998) 3–16, https://doi.org/10.1016/S0302-4598(97)00093-7.
[39] A. Irimajiri, T. Suzaki, K. Asami, T. Hanai, Dielectric modeling of biological cells : models and algorithm, Bull. Inst. Chem. Res. Kyoto. 69 (1991) 421–438.
[40] D. Das, F.A. Kamil, K. Biswas, S. Das, Evaluation of single cell electrical parameters from bioimpedance of a cell suspension, RSC Adv. 4 (35) (2014) 18178–18185, https://doi.org/10.1039/C4RA00400K.
[41] E.K. Moen, H.T. Beier, G.L. Thompson, A.M. Armani, B.L. Ibey, Nonlinear imaging of lipid membrane alterations elicited by nanosecond pulsed electric fields, in: Energy-Based Treat. Tissue Assess. VIII, 2015: p. 93260T. https://doi.org/10.1117/12.2079452.
[42] A.G. Pakhomov, J.F. Kolb, J.A. White, R.P. Joshi, S. Xiao, K.H. Schoenbach, Long-lasting plasma membrane permeabilization in mammalian cells by nanosecond Pulsed Electric Field (nsPEF), Bioelectromagnetics. 28 (8) (2007) 655–663, https://doi.org/10.1002/(ISSN)1521-186X10.1002/bem.v28:810.1002/bem.20354.
[43] B.L. Ibey, S. Xiao, K.H. Schoenbach, M.R. Murphy, A.G. Pakhomov, Plasma membrane permeabilization by 60- and 600-ns electric pulses is determined by the absorbed dose, Bioelectromagnetics. 30 (2) (2009) 92–99, https://doi.org/10.1002/bem.v30:210.1002/bem.20451.
[44] E.W. Miller, J.Y. Lin, E.P. Frady, P.A. Steinbach, W.B. Kristan, R.Y. Tsien, Optically monitoring voltage in neurons by photoinduced electron transfer through molecular wires, Proc. Natl. Acad. Sci. U. S. A. 109 (6) (2012) 2114–2119, https://doi.org/10.1073/pnas.1120694109.
[45] E. Tekle, R.D. Astumian, P.B. Chock, Selective and asymmetric molecular transport across electroporated cell membranes, Proc. Natl. Acad. Sci. U. S. A. 91 (24) (1994) 11512–11516, https://doi.org/10.1073/pnas.91.24.11512.
[46] B.L. Ibey, J.N. Bixler, C.C. Roth, H.T. Beier, Evaluation of membrane potential changes induced by unipolar and bipolar nanosecond pulsed electric fields, in, Proc.SPIE (2019) 39, https://doi.org/10.1117/12.2511189.
[47] B.L. Ibey, D.G. Mixon, J.A. Payne, A. Bowman, K. Sickendick, G.J. Wilmink, W.P. Roach, A.G. Pakhomov, Plasma membrane permeabilization by trains of ultrashort electric pulses, Bioelectrochemistry 79 (1) (2010) 114–121, https://doi.org/10.1016/j.bioelechem.2010.01.001.
[48] Z.A. Steelman, G.P. Tolstykh, H.T. Beier, B.L. Ibey, Cellular response to high pulse repetition rate nanosecond pulses varies with fluorescent marker identity, Biochem. Biophys. Res. Commun. 478 (3) (2016) 1261–1267, https://doi.org/10.1016/j.bbrc.2016.08.107.
[49] A.G. Pakhomov, S. Xiao, V. Novickij, M. Casciola, I. Semenov, U. Mangalanathan, V. Kim, C. Zemlin, E. Sozer, C. Muratori, O.N. Pakhomova, Excitation and electroporation by MHz bursts of nanosecond stimuli, Biochem. Biophys. Res. Commun. 518 (4) (2019) 759–764, https://doi.org/10.1016/j.bbrc.2019.08.133.
[50] A. Silve, I. Leray, C. Poignard, L.M. Mir, Impact of external medium conductivity on cell membrane electropermeabilization by microsecond and nanosecond electric pulses, Sci. Rep. 6 (1) (2016), https://doi.org/10.1038/srep19957.
[51] C. Merla, M. Liberti, F. Apollonio, G. D'inzeo, Quantitative assessment of dielectric parameters for membrane lipid bi-layers from rf permittivity measurements, Bioelectromagnetics. 30 (4) (2009) 286–298, https://doi.org/10.1002/bem.v30:410.1002/bem.20476.
[52] M.M.M. Elnasharty, A.M. Ghoneim, G.M. Turky, M. Kamal, K. Hoettges, F.H. Labeed, M.P. Hughes, Conductivity of cell membrane investigated by a novel dielectrophoretic technique, Biotechnol. An Indian J. 7 (2013) 60–70.
[53] M. Pavlin, M. Kandušer, M. Reberšek, G. Pucihar, F.X. Hart, R. Magjarevićcacute;, D. Miklavčič, Effect of cell electroporation on the conductivity of a cell suspension, Biophys. J. 88 (6) (2005) 4378–4390, https://doi.org/10.1529/biophysj.104.048975.
[54] W. Liang, Y. Zhao, L. Liu, Y. Wang, W.J. Li, G. Bin Lee, Determination of cell membrane capacitance and conductance via optically induced electrokinetics, Biophys. J. 113 (2017) 1531–1539. https://doi.org/10.1016/j.bpj.2017.08.006.
[55] E.K. Moen, B.L. Ibey, H.T. Beier, Detecting subtle plasma membrane perturbation in living cells using second harmonic generation imaging, Biophys. J. 106 (2014). https://doi.org/10.1016/j.bpj.2014.04.008.
[56] E.K. Moen, B.L. Ibey, H.T. Beier, A.M. Armani, Investigating membrane nanoporation induced by bipolar pulsed electric fields via second harmonic generation, Appl. Phys. Lett. 109 (2016) 113701. https://doi.org/10.1063/1.4962839.